SOLA (2026) 22:11
https://doi.org/10.1007/s44393-025-00010-y

BRIEF REPORT

Zonal Asymmetry of the Quasi-Biennial Oscillation

Ryo Hayakawa[1] · **Yoshio Kawatani**[2]

Received: 29 September 2025 / Accepted: 31 December 2025

Abstract
Zonal asymmetry in the amplitude of the Quasi-Biennial Oscillation (QBO) is investigated using JRA-55 reanalysis data and in-situ IGRA radiosonde observations. In addition to the previously reported asymmetry near 10 hPa, significant longitudinal variation with the largest amplitudes over the western and central Pacific is found around 70 hPa. Unlike the dominant wavenumber-1 pattern near 10 hPa, the structure at 70 hPa exhibits more localized variations. Longitudinal differences in the QBO zonal wind at 70 hPa reach up to 30%, indicating that the descent of the QBO into the lower stratosphere and upper troposphere exhibits pronounced longitudinal variation. The asymmetry results were confirmed in five additional reanalysis datasets. Similar zonal variation of QBO amplitudes is also identified in radiosonde observations and in both CMIP6 and QBOi models that explicitly simulate the QBO. These results demonstrate that the longitudinal structure of the 70-hPa QBO amplitude is a robust feature across observations, reanalyses, and climate models.

Keywords Quasi-biennial oscillation (QBO) · Stratosphere–troposphere coupling · El Niño–Southern Oscillation (ENSO) · QBOi · CMIP6 · Reanalysis · Zonal asymmetry

1 Introduction

The Quasi-Biennial Oscillation (QBO) is the dominant mode of interannual variability in the tropical stratosphere, characterized by alternating easterly and westerly zonal winds with a mean period of about 28 months (Baldwin et al. 2001; Anstey et al. 2022). While the QBO has traditionally been considered a zonally symmetric phenomenon, several studies have indicated the presence of longitudinal asymmetries. The observed zonally asymmetric structures in the equatorial middle stratosphere (around 10 hPa) can be characterized fairly simply. Notably winter hemisphere mid-latitude planetary waves (primarily zonal wavenumber-1) penetrate into the equatorial region during the westerly phase of the QBO (Hamilton et al. 2004; Kawatani et al. 2016) but not during the easterly phase. More recently, Sakazaki and Hamilton (2022) refined this picture by identifying quasi-stationary wavenumber-1 equatorially trapped Rossby and Kelvin wave structures which sometimes appear near 10 hPa in the peak westerly and easterly QBO jets.

While these studies have focused on the QBO in the middle stratosphere, the simple wavenumber-1 dominated picture does not apply below ~20 hPa (Hamilton et al. 2004), and zonally asymmetric structures in the lower stratosphere have received comparatively less attention. Understanding the zonal variation of QBO circulation in the lower stratosphere is important as this region connects most directly with tropospheric variability. In particular, recent studies have indicated that QBO variations of lower-stratospheric circulation may be linked to the activity of tropical cyclones, the Asian monsoon and the Madden–Julian Oscillation (e.g., Ho et al. 2009; Seo et al. 2013; Yoo and Son 2016; Ju et al. 2025).

The present study examines the structure of prevailing zonal wind variations associated with the QBO, focusing on their longitudinal, vertical, and QBO phase dependence, with particular emphasis on the 70-hPa level. The primary analysis is based on the JRA-55 reanalysis, with near equatorial radiosonde observations. Additionally, five reanalyses and climate-model simulations are used to assess the robustness of the identified features.

✉ Yoshio Kawatani
kawatani@ees.hokudai.ac.jp

[1] Graduate school of Environmental Science, Hokkaido University, Sapporo, Japan

[2] Faculty of Environmental Earth Science, Hokkaido University, N10 W5 Kita-ku, Sapporo 060- 0810, Japan

Published online: 05 February 2026

2 Data and Study Method

Monthly mean zonal wind (u) data from the JRA-55 reanalysis (Kobayashi et al. 2015) were used, with a horizontal resolution of 1.25° and 37 pressure levels from 1000 to 1 hPa. Data from January 1958 to December 2015 were analyzed, which excludes the QBO disruption events (Osprey et al. 2016; Newman et al. 2016; Wang et al. 2023, 2025) in early 2016 and during 2019/20 boreal winter to focus on the fundamental QBO structures in their undisturbed state. Some calculations were also repeated using the ERA5 (Hersbach et al. 2020), ERA-Interim (Dee 2011), MERRA (Rienecker et al. 2011), MERRA-2 (Gelaro et al. 2017), and NCEP-CFSR (Saha et al. 2010) reanalyses, in each case considering data from January 1980 to December 2015 (note that MERRA-2 are available only after 1980 and NCEP-CFSR are available until 2010).

Two different versions of each time series were processed with different filtering applied to isolate the QBO signal. The first filter follows Dunkerton and Delisi (1985; hereinafter "DD"). It removes the climatological annual cycle from the raw time series at each level, and applies a 5-month running mean to smooth the data, resulting in a filtered time series denoted as "U_{DD}". The second filter applies a Fast Fourier Transform (FFT) to the raw data to extract components with periods between 18 and 36 months and resulting in a filtered time series denoted as "U_{FFT}".

While the DD method is designed to include the rapid non-sinusoidal variations in the QBO evolution, it may also retain longer-period signals. The FFT method removes such long-period variability but tends to smooth over the values during the rapid QBO transitions, leading to generally smaller estimates of the QBO amplitude than obtained using the DD filtering.

From the U_{DD} and U_{FFT} filtered series of JRA-55 zonal mean equatorial 20-hPa winds, the months of both westerly-to-easterly (WE) and easterly-to-westerly (EW) transitions were identified separately for each filtering method (dates listed in the Supplementary Tables S1-S3). These dates were used both in the construction of QBO composites (see below) and to define a series of individual QBO cycles at each grid point in longitude, latitude and pressure level, each cycle being the interval from one transition month to the month before the next transition of the same type during 1958–2015. For each of the filtered time series the standard deviation σ_u was calculated for each QBO cycle, and the QBO amplitude for that cycle estimated as $A_u = \sqrt{2}\sigma_u$. The climatological QBO amplitude was then calculated by averaging the amplitudes over all 24 EW QBO cycles. Hereafter, "QBO amplitude" denotes this cycle-based diagnostic. In the upper troposphere, it may include variability other than the QBO and is interpreted accordingly.

For composite analysis, WE and EW transitions identified from each filtering method were used as reference months. The filtered wind series were composited separately for EW and WE transitions using a ± 18-month window centered on the transition month. Because of this window length, the first of both EW and WE, and the last of EW transitions in the record could not be employed as reference months. Consequently, composites are based on 23 cycles for EW and 24 cycles for WE.

Radiosonde observations from the Integrated Global Radiosonde Archive (IGRA) v2.2 archive (Durre et al. 2016) were also analyzed to provide another observational perspective. Monthly mean zonal wind data at 70 hPa from stations within ± 10° latitude were used. QBO amplitudes were calculated using the DD method, and only stations with sufficient temporal coverage were retained. The detailed processing procedures are described in the Supplementary Section S1.

Climate-model simulations were also analyzed. CMIP6 historical simulations from QBO-resolving models (cf. Richter et al. 2020; Rao et al. 2020a, b) and the QBOi experiment 1 and experiment 2 (Butchart et al. 2018) integrations were processed using the same diagnostics as for the reanalyses (see Supplementary Sections S3 and S4).

3 Results

Figure 1 presents time-height cross-sections of the composite zonal wind U_{DD} over the equator at 0°E and 180°E, along with their difference (180ºE minus 0ºE) presented for EW and WE transitions. Two largest differences are concentrated in two layers near 10 hPa and 70 hPa, with larger contrasts near 70 hPa for both cases. The zonal differences around 70-hPa peak when the QBO extends most strongly into the lowermost stratosphere, reaching up to 2.4 m s^{-1} relative to zonal mean zonal winds of ~ 8 m s^{-1}, corresponding to a variation of about 30%. Similar features are also seen in zonal wind composites based on U_{FFT} (Fig. S1).

Figure 2a-d show the geographical distribution of the climatological QBO amplitude at 10 hPa and 70 hPa calculated using U_{DD}, along with deviations from the zonal mean. At each location amplitude deviations were calculated for each QBO cycle, and a Student's t-test was applied over all 24 cycles to assess statistical significance. Stippling indicates regions significant at the 95% confidence level. At 10 hPa,

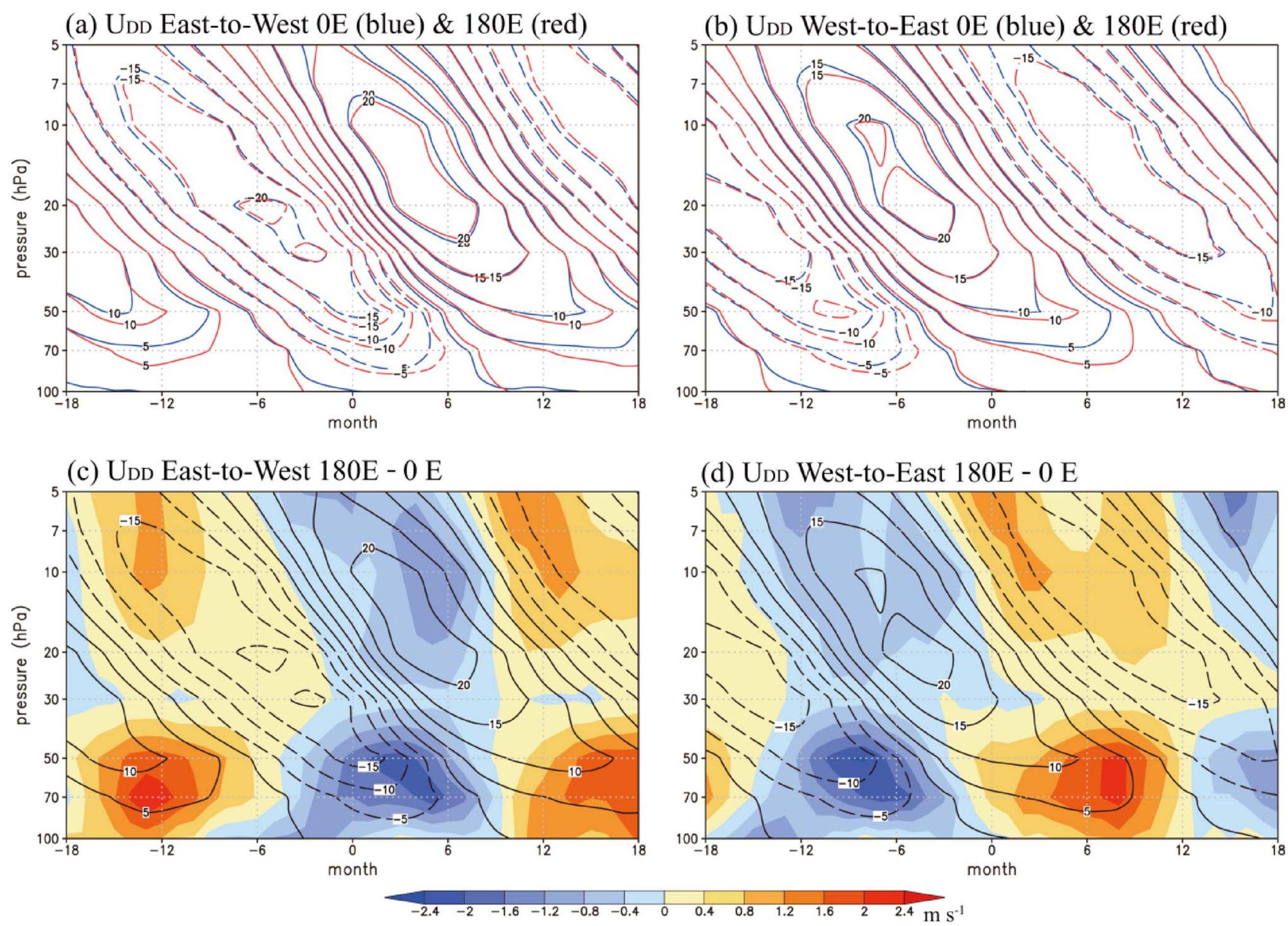

Fig. 1 Time–height cross-sections of the composite QBO zonal wind over the equator, derived by applying DD filtering to JRA-55 monthly mean time series (U_{DD}). Upper panels show composites for the QBO phase transition: (**a**) easterly-to-westerly and (**b**) westerly-to-easterly at 20 hPa, with month 0 denoting the transition month. The composites cover ± 18 months from month 0. Blue and red contours indicate zonal wind at 0°E and 180°E, respectively, with a contour interval of 5 m s⁻¹. Lower panels show the difference (180°E minus 0°E) for the corresponding phases, with black contours indicating zonal mean zonal wind (contour interval: 5 m s⁻¹) and shading showing the difference (color interval: 0.5 m s⁻¹)

QBO amplitude over the equator is larger over a sector stretching east from the Atlantic to the western Pacific, while amplitude is smaller over central to eastern Pacific. There is a clear wavenumber-1 pattern in the deviation from the zonal mean (Fig. 2a, c). In contrast, at 70 hPa, the equatorial QBO amplitude is significantly enhanced from the Maritime Continent to the central Pacific, with additional small peaks over Africa and South America (Fig. 2b). The largest positive anomalies are somewhat narrowly confined in the western and central Pacific (Fig. 2 d).

Figure 2e and f show longitude-height cross-sections of QBO amplitude anomalies from the zonal mean, calculated from U_{DD} and U_{FFT}. A clear wavenumber-1 structure is present in the middle stratosphere, with maximum near 10 hPa, consistent with previous studies (Hamilton et al. 2004; Sakazaki and Hamilton 2022). Zonally asymmetric structures are also evident around 70 hPa, particularly between 140°E and 140ºW, indicating a more localized zonal structure compared to that around 10 hPa. In both methods, stronger anomalies are found in the upper troposphere, peaking particularly near 150 hPa around 150°W. These features will be discussed further in connection with Fig. 4 below.

Figure 3a-d present longitude-time cross-sections of the EW and WE transition composite zonal wind U_{DD} and its deviation from the zonal mean at 10 hPa and 70 hPa. At 10 hPa, a zonal wavenumber-1 pattern is evident, with relatively strong westerlies (easterlies) over the Eastern Hemisphere during the westerly (easterly) phase and weaker

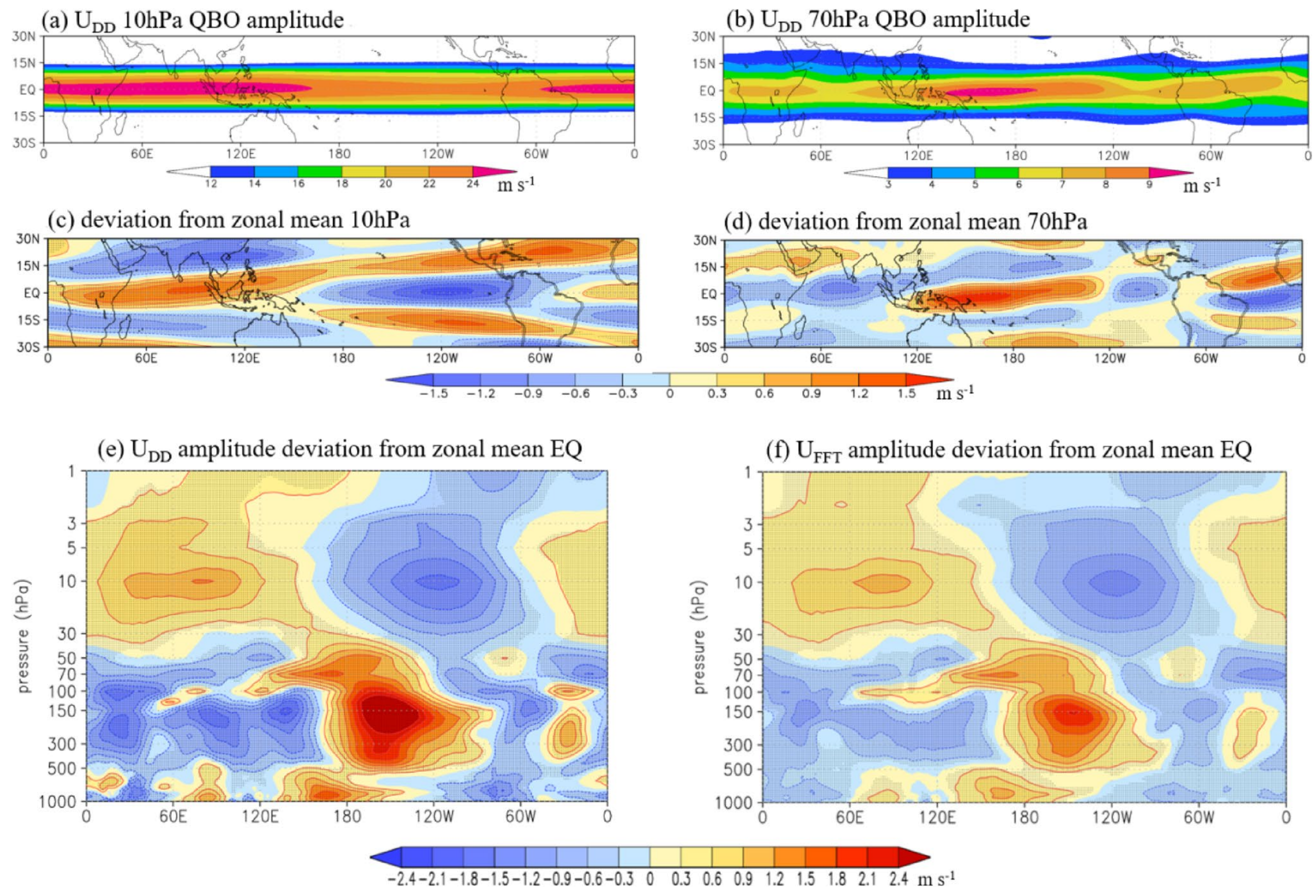

Fig. 2 Horizontal distributions of (**a**, **b**) QBO amplitude and (**c**, **d**) deviation from the zonal mean at 10 hPa (**a**, **c**) and 70 hPa (**b**, **d**), calculated using the DD method. Panels (**e**) and (**f**) show longitude–height cross-sections of the QBO amplitude deviation from the zonal mean over the equator, calculated using the DD method (**e**) and the FFT method (**f**). The color interval is 2 m s^{-1} in (**a**), 1 m s^{-1} in (**b**), and 0.3 m s^{-1} in (**c**, **d**). Stippling indicates regions that are statistically significant at the 95% confidence level

westerlies (easterlies) over the eastern Pacific, resulting in a clear wavenumber-1 contrast in amplitude. In contrast, at 70 hPa, stronger westerlies (easterlies) are found over the western and central Pacific during the westerly (easterly) phases, with the strongest anomalies confined between approximately 120°E and 130°W, exhibiting a more localized structure than at 10 hPa. Similar features are also found based on U_{FFT} (Fig. S2).

Figure 3e and f shows time–height cross-sections of the longitudinal standard deviation of the composite U_{DD}, along with the corresponding zonal-mean zonal wind composite, for both transition types. Peaks in longitudinal standard deviation appear around 10 hPa and 70 hPa during both transition phases. Between 50 and 100 hPa, substantial standard deviations are seen near the lowest altitudes to which the QBO westerly or easterly phases descend, indicating that the QBO penetration into the lowermost stratosphere depends significantly on longitude. These characteristics are also confirmed by the composites based on U_{FFT} (Fig. S3).

The QBO amplitude deviations from the zonal mean, calculated using both U_{FFT} and U_{DD} (Fig. 2e and f), show pronounced positive anomalies over the western and central Pacific around 70 hPa. Additional large positive anomalies are also evident in the troposphere above 500 hPa, with a maximum near 150 hPa around 150°W. Two amplitude peaks at 70 hPa and 150 hPa appear as distinct maxima.

To further investigate these peaks, frequency–height cross-sections of the power spectra were examined (Fig. S4), based on U_{DD} at 0°E and 150°W, and U_{FFT} at 150°W. In the stratosphere, QBO components are well captured in U_{DD}, but spectral power also appears at longer periods (e.g., 42–84 months), which are likely unrelated to the QBO. In the troposphere, these long-period components are weak at 0°E but more prominent at 150°W. Spectral power in the

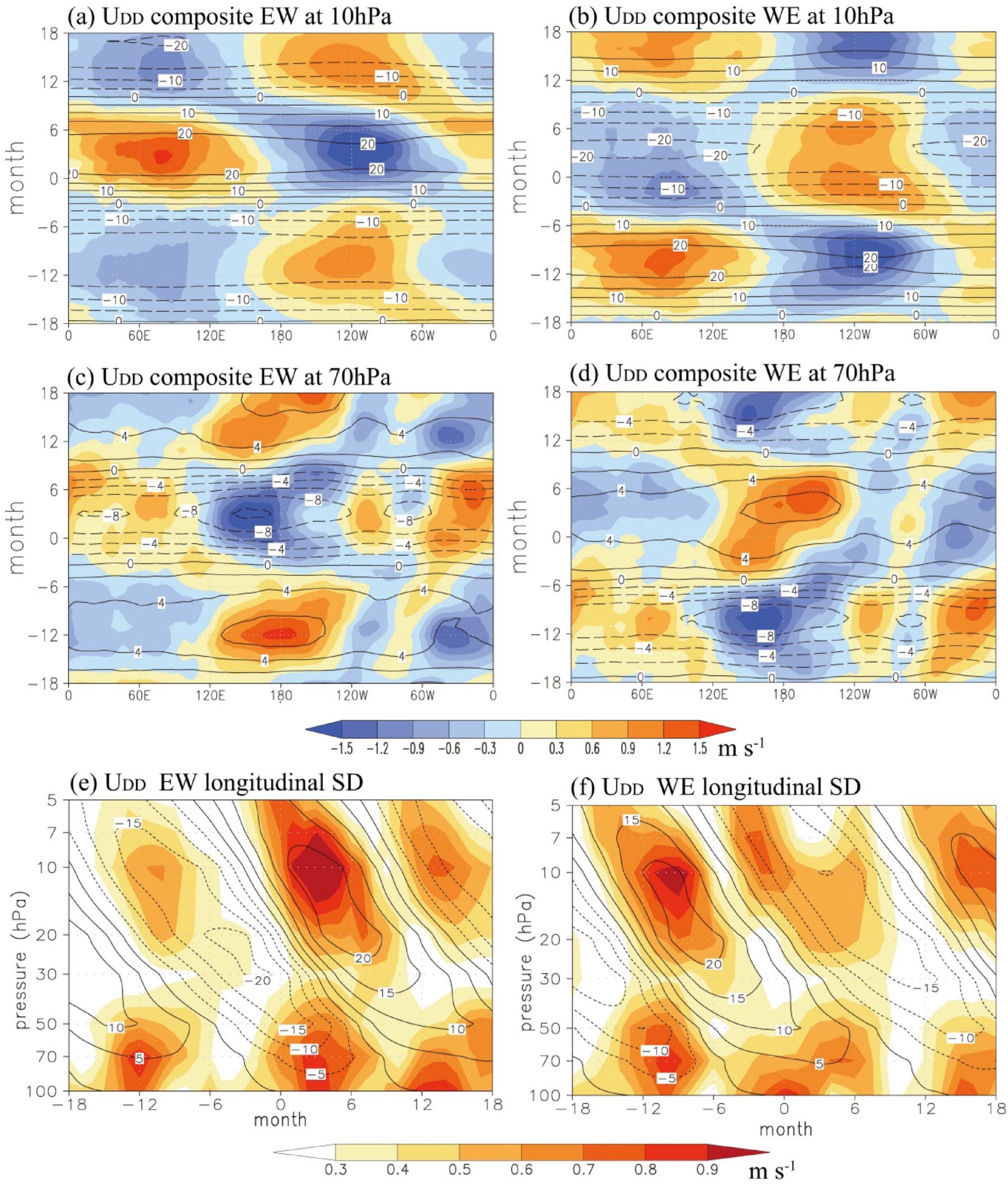

Fig. 3 (**a**-**d**) Longitude–time cross-sections of the composite deviations of U_{DD} from the zonal mean at (**a**,**b**) 10 hPa and (**c**, **d**) 70 hPa. Month 0 denotes the QBO phase transition at 20 hPa: (**a**, **c**) easterly-to-westerly and (**b**, **d**) westerly-to-easterly. Black contours show the composite U_{DD}, with a contour interval of 2 m s⁻¹. The color interval is 0.3 m s⁻¹. (**e**, **f**) Time–height cross-sections of the longitudinal standard deviation of composite U_{DD}, where larger values indicate stronger zonal asymmetry. Contours indicate the composite zonal-mean U_{DD} with a contour interval of 5 m s⁻¹. The color interval is 0.1 m s⁻¹, starting from 0.3 m s⁻¹. Panel (**e**) corresponds to the easterly-to-westerly phase at 20 hPa, and panel (**f**) to the westerly-to-easterly transition

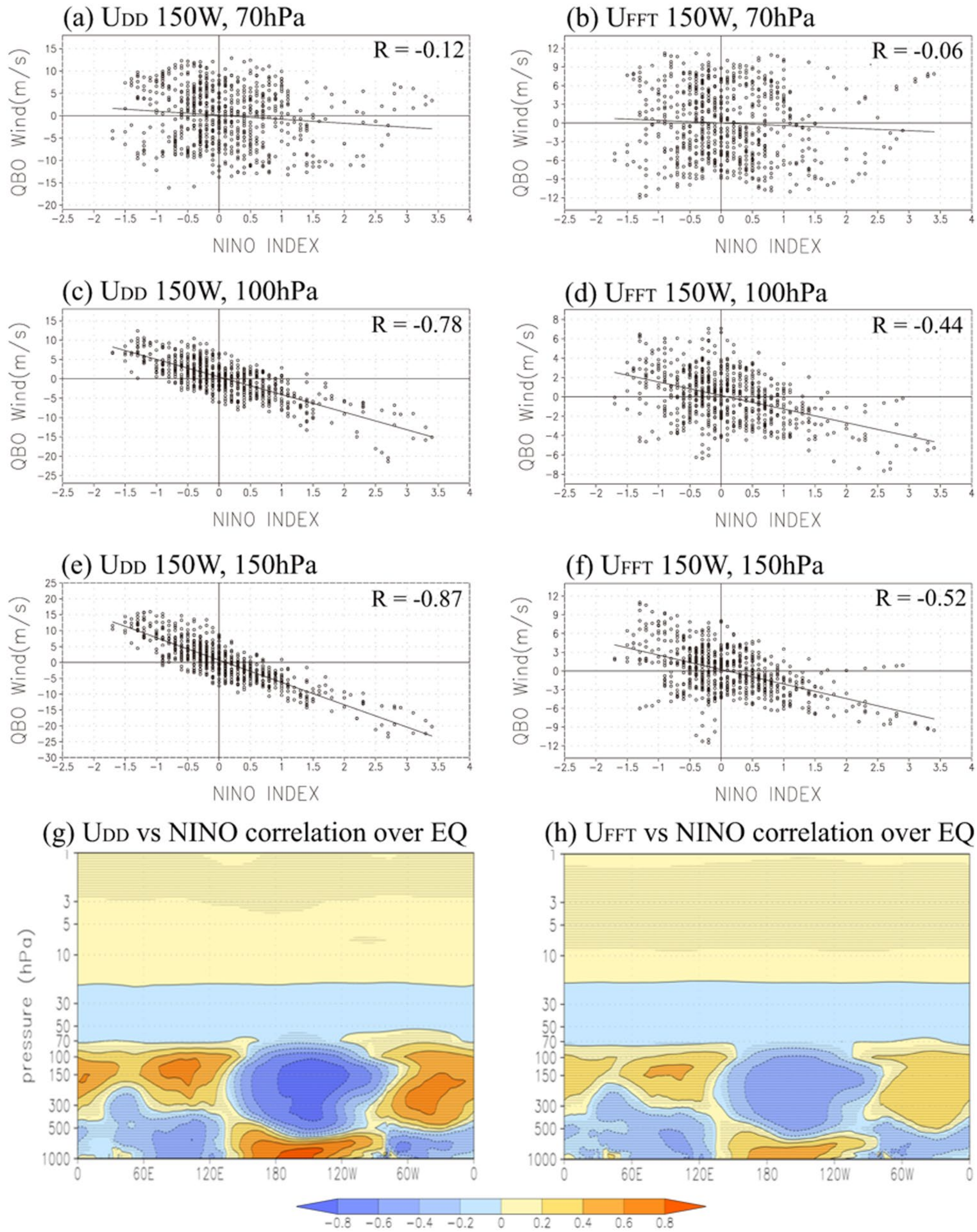

Fig. 4 Scatter plots of the Niño3 index versus QBO-related zonal wind component U_{DD} (left column) and its FFT-filtered counterpart U_{FFT} (right column) at 70 hPa (**a**, **b**), 100 hPa (**c**, **d**), and 150 hPa (**e**, **f**). The correlation coefficient is shown in each panel. Panels (**g**) and (**h**) present longitude–height cross-sections of the correlation between the Niño index and U_{DD} or U_{FFT} over the equator. Stippling indicates regions that are statistically significant at the 95% confidence level

18–36 month range is also considerably stronger at 150°W than at 0°E below about 150 hPa, raising the question of whether this signal originates from the QBO or is associated with ENSO. In contrast to U_{DD}, U_{FFT} effectively eliminates signals with periods longer than 36 months and shorter than 18 months, thereby isolating the typical QBO periodic components.

To clarify the possible role of ENSO in producing the "QBO" amplitude peaks at 70 hPa and 150 hPa in the Pacific, correlations were calculated separately between the monthly NINO3 index defined by the Japan Meteorological Agency and both U_{DD} and U_{FFT}. Fig. 4a–f are scatter plots of the NINO3 index versus U_{DD} or U_{FFT} at 150°W at 70, 100 and 150 hPa. At 150 and 100 hPa, clear negative correlations of about −0.8 are evident in U_{DD}. Although the magnitudes are smaller, clear negative correlations are also found in U_{FFT}. At 100 hPa, the relationship between U_{FFT} and NINO3 is unclear when the index is within ±1. However, stronger

ENSO events appear to contribute more clearly to the negative correlation. In contrast, the correlations at 70 hPa are −0.1 for U_{DD} and close to zero for U_{FFT}, suggesting that the zonal asymmetry at this level is primarily attributable to the QBO itself rather than to ENSO variability.

Figure 4g and h present the longitude–height cross-section of the correlation between NINO3 index and both U_{DD} and U_{FFT}. Statistically significant correlations exceeding 0.2 in magnitude are found throughout the troposphere, even for U_{FFT}, whereas correlations above 70 hPa are generally negligible. These results indicate that the zonal asymmetry of the QBO amplitude at 70 hPa is not influenced by ENSO.

To further examine the spatial distribution of 70-hPa QBO amplitude, radiosonde observations from IGRA v2.2 were analyzed. Stations with complete data for more than 8 out of 24 QBO cycles during 1958–2015 were selected, and QBO amplitude at each station were estimated using the DD method (see Methods in Supplementary Section S1 for details). Figure 5a shows the latitudinal distribution of individual climatological QBO amplitudes at 70 hPa, along with the JRA-55 zonal-mean climatology and the $\pm 1\sigma$ and $\pm 2\sigma$ envelopes, where σ represents the longitudinal standard deviation of climatological QBO amplitude at each latitude. Most stations fall within the $\pm 2\sigma$ envelope of the JRA-55 zonal-mean climatology.

Figure 5b shows the radiosonde stations within ±10° latitude that met the minimum data coverage threshold. Stations with over 90% coverage are concentrated over Singapore and near 7–9°N in the western–central Pacific, while coverage is much sparser elsewhere (Kawatani and Hamilton 2013). The QBO amplitude exhibits a strong meridional dependence, peaking at the equator with a typical half-width of about 12° latitude (Baldwin et al. 2001). For each station, an "adjusted" amplitude was also computed to represent to an equivalent equatorial value. This latitudinal correction was based on the zonal-mean meridional profile of the QBO amplitude derived from JRA-55 data, and was used to normalize amplitude estimates across stations at different latitudes. The resulting equator-adjusted amplitudes enable fairer comparisons of longitudinal structure.

Although a strict comparison of climatological amplitudes would require averaging over identical observation periods at all stations, as cycle-to-cycle variability and a long-term negative trend in QBO amplitude have been reported (Kawatani and Hamilton 2013), averaging over at least 8 cycles provides a more consistent basis for comparison across stations. These stations shown in Fig. 5b therefore offer a reasonable basis for examining the longitudinal structure.

Figure 5c shows the longitudinal distribution of the adjusted climatological amplitudes and the corresponding amplitude for individual QBO cycles, revealing substantial cycle-to-cycle variability at most stations. The sharp amplitude contrast (approximately 3 m s^{-1}) across a narrow longitudinal band between about 100°E and 120°E is primarily due to the particularly low value at KOTA BHARU (station 6) and high value at JUANDA (station 10). Nevertheless, longitudinal variations in 70-hPa QBO amplitude are also evident in the radiosonde data, showing increased amplitude from 100°E toward the central Pacific, followed by a decrease toward the eastern Pacific and a secondary increase near South America. Despite the limited spatial coverage, the selected radiosonde observations provide support for the presence of longitudinal asymmetry in the 70-hPa QBO amplitude.

In addition, the basic computation of 70-hPa QBO amplitude was repeated using five additional reanalysis datasets: ERA5, ERA-Interim, MERRA, MERRA-2, and NCEP-CFSR in addition to JRA-55, for the period 1980–2015 (with MERRA-2 data available only after 1980 and with NCEP-CFSR available until 2010). Fig. 6a-f show the same diagnostics as Fig. 2d. Note that the results using JRA-55 data during 1980–2015 (Fig. 6c) are very similar to those for the entire 1958–2015 period. All datasets exhibit quite similar patterns of zonal asymmetry at 70 hPa, although the MERRA-2 results notably have a somewhat weaker western Pacific maximum.

To assess consistency with the radiosonde observations, the 70-hPa QBO amplitudes in each reanalysis were interpolated to the same 27 station locations and processed using identical methods. Fig. 6g shows the longitudinal variations of the 70-hPa QBO amplitude for each reanalysis together with the radiosonde estimates (same as the upper panel of Fig. 5c). Each reanalysis closely matches the radiosonde results at the 27 stations. When the amplitudes were evaluated at all equatorial longitudes (Fig. 6h), the reanalyses consistently exhibited three distinct longitudinal peaks, with maxima over the western–central Pacific, a weaker enhancement near Africa, and another peak near South America, despite some spread among the datasets. Supplementary Figs. S5 and S6 further demonstrate that the zonal-mean (symmetric) components and the longitudinal-deviation

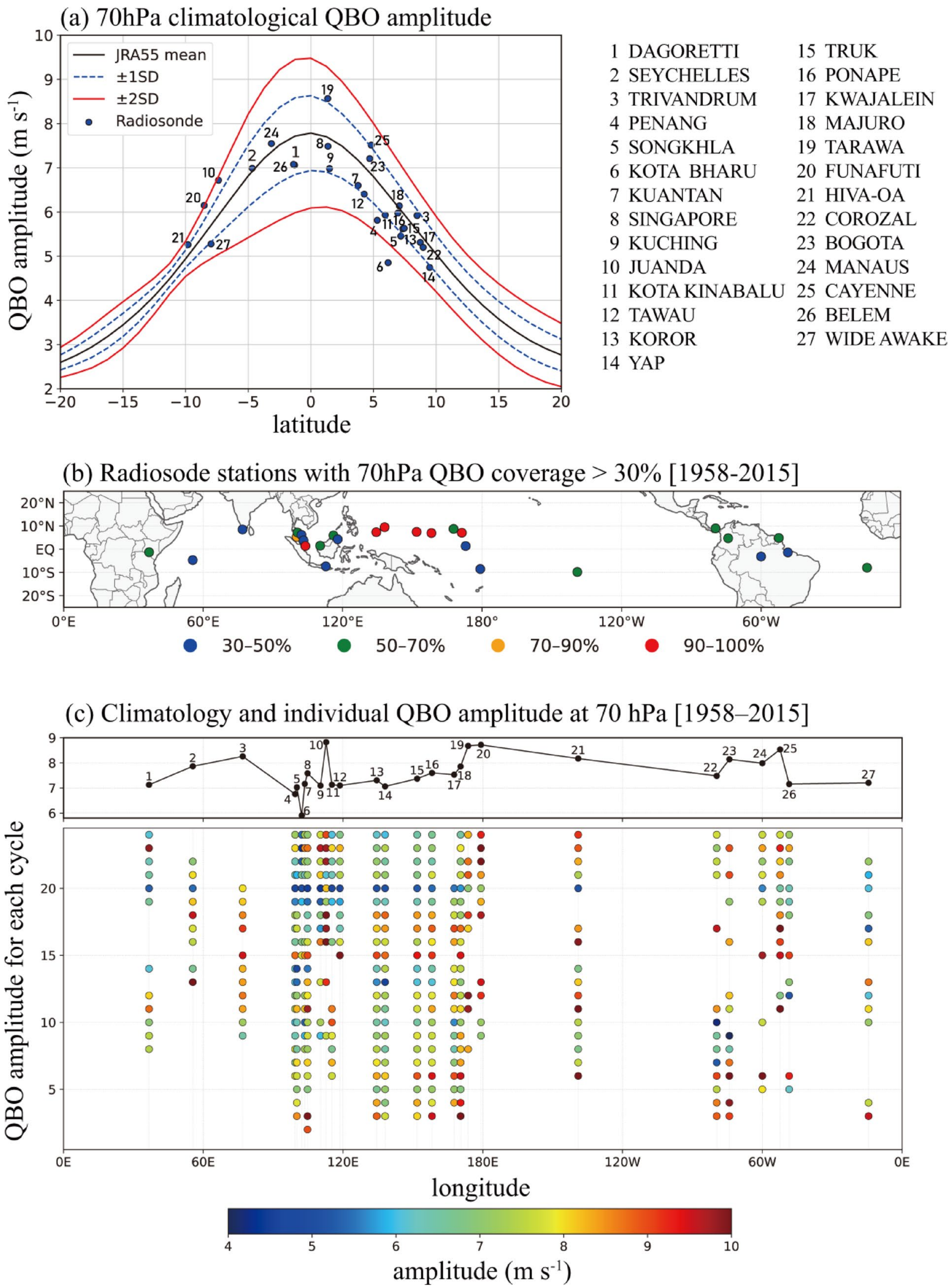
(a) 70hPa climatological QBO amplitude
JRA55 mean
±1SD
±2SD
Radiosonde
QBO amplitude (m s-1)
latitude
1 DAGORETTI
2 SEYCHELLES
3 TRIVANDRUM
4 PENANG
5 SONGKHLA
6 KOTA BHARU
7 KUANTAN
8 SINGAPORE
9 KUCHING
10 JUANDA
11 KOTA KINABALU
12 TAWAU
13 KOROR
14 YAP
15 TRUK
16 PONAPE
17 KWAJALEIN
18 MAJURO
19 TARAWA
20 FUNAFUTI
21 HIVA-OA
22 COROZAL
23 BOGOTA
24 MANAUS
25 CAYENNE
26 BELEM
27 WIDE AWAKE
(b) Radiosode stations with 70hPa QBO coverage > 30% [1958-2015]
30-50%
50-70%
70-90%
90-100%
(c) Climatology and individual QBO amplitude at 70 hPa [1958–2015]
QBO amplitude for each cycle
longitude
amplitude (m s-1)

Fig. 5 (**a**) Latitudinal structure of the climatological QBO amplitude at 70 hPa from JRA-55 data for 1958–2015. The black solid curve denotes the zonal-mean amplitude, while the blue dashed and red solid curves indicate ± 1σ and ± 2σ envelopes of the longitudinal standard deviation, respectively. Filled circles show climatological amplitudes derived from radiosonde observations at each station, with station numbers labeled on the right. (**b**) Location of radiosonde stations within ± 10° latitude with at least 30% data coverage for estimating the 70-hPa QBO amplitude during 1958–2015. Marker color denotes the fraction of QBO cycles with complete 70-hPa data (30–50%, 50–70%, 70–90%, 90–100%). (**c**) Longitudinal distribution of 70-hPa QBO amplitudes, showing the climatological average for each station (top; with station numbers) and amplitudes from individual QBO cycles (bottom; colored dots). The y-axis in the top panel shows the station climatological amplitude. In the bottom panel, the vertical axis indicates the individual QBO cycle number (out of 24 cycles during 1958–2015) at each station, defined by successive easterly-to-westerly transitions listed in Table S3, while the color scale represents the QBO amplitude for each cycle

(asymmetric) components derived from these fields have comparable magnitudes across datasets.

The longitudinal structure is also examined in climate-model simulations. The multi-model means of CMIP6 and the QBOi experiments (Fig. 7a–d) show enhanced QBO amplitudes over the western–central Pacific at 70 hPa, consistent with the reanalysis results. Longitude–height sections (Fig. 7e–h) reveal a pronounced peak near 150 hPa and 150°W in CMIP6 and in QBOi experiment 1, but not in experiment 2. Because CMIP6 and QBOi experiment 1 include interannually varying SSTs (and therefore ENSO variability), whereas experiment 2 uses climatological SSTs without ENSO variations, this contrast strongly supports the interpretation from Fig. 4 that this signal is primarily ENSO-related rather than part of the QBO. Details of individual models and additional explanations are provided in the Supplementary Sections S3 and S4.

4 Summary and Discussion

This study investigated the longitudinal variations of the QBO amplitude in the lower stratosphere, with a particular focus on the 70-hPa level, using JRA-55 and five additional reanalysis datasets, as well as radiosonde observations from the IGRA v2.2 archive. Two methods were applied to extract the QBO signal: one following Dunkerton and Delisi (1985), and the other using FFT spectral decomposition. Both methods generally produced similar overall structures.

While previous studies have demonstrated pronounced zonal asymmetry of QBO amplitude near 10 hPa (Hamilton et al. 2004; Kawatani et al. 2016; Sakazaki and Hamilton 2022), the longitudinal structure of the QBO in the lower stratosphere, especially near 70 hPa, has not been well documented. The present results revealed that at 70 hPa, the QBO amplitude displays significant zonal asymmetry, characterized by a maximum over the western and central Pacific. This longitudinal pattern was consistently identified across all reanalysis products, despite differences in model formulation and data assimilation systems.

Radiosonde observations from IGRA were also analyzed to provide an additional observational perspective. Stations with sufficient temporal coverage to estimate reliable QBO amplitude climatology were selected. After scaling the station amplitudes to the equator to account for the meridional structure of the QBO, the IGRA results showed a clear longitudinal variation.

The 70-hPa QBO amplitudes derived from each reanalysis, interpolated to the 27 station locations, show longitudinal variations similar to the radiosonde observations, with zonal-mean (symmetric) and longitudinal-deviation (asymmetric) components of comparable magnitude across datasets. Evaluated over all equatorial longitudes, the reanalyses exhibit a consistent three-peak pattern, with a dominant maximum over the western–central Pacific, a smaller enhancement near Africa, and another peak near South America, although some spread in magnitude is present.

In addition to the amplitude maximum at 70 hPa over the western and central Pacific, large signals extracted by the QBO filtering methods were also found near 150 hPa around 150°W. Correlation analyses between the NINO3 index and the QBO components of zonal wind (U_{DD} and U_{FFT}) revealed strong link at this level, suggesting an influence of ENSO variability. In contrast, correlations at 70 hPa were negligible, indicating that the QBO zonal asymmetry is not much influenced by ENSO effects.

The longitudinal asymmetry of QBO-related temperature anomalies near the cold-point tropopause and at 100 hPa, as reported by Tegtmeier et al. (2020), featured maxima over the Eastern Hemisphere. These anomalies likely reflect both QBO dynamical effects and convective influences. In contrast, the zonal wind amplitude analyzed in this study, primarily representing the dynamical QBO descent, shows a western and central Pacific maximum. This contrast highlights the need to analyze zonal wind fields alongside temperature data for a more complete understanding of the QBO's longitudinal structure.

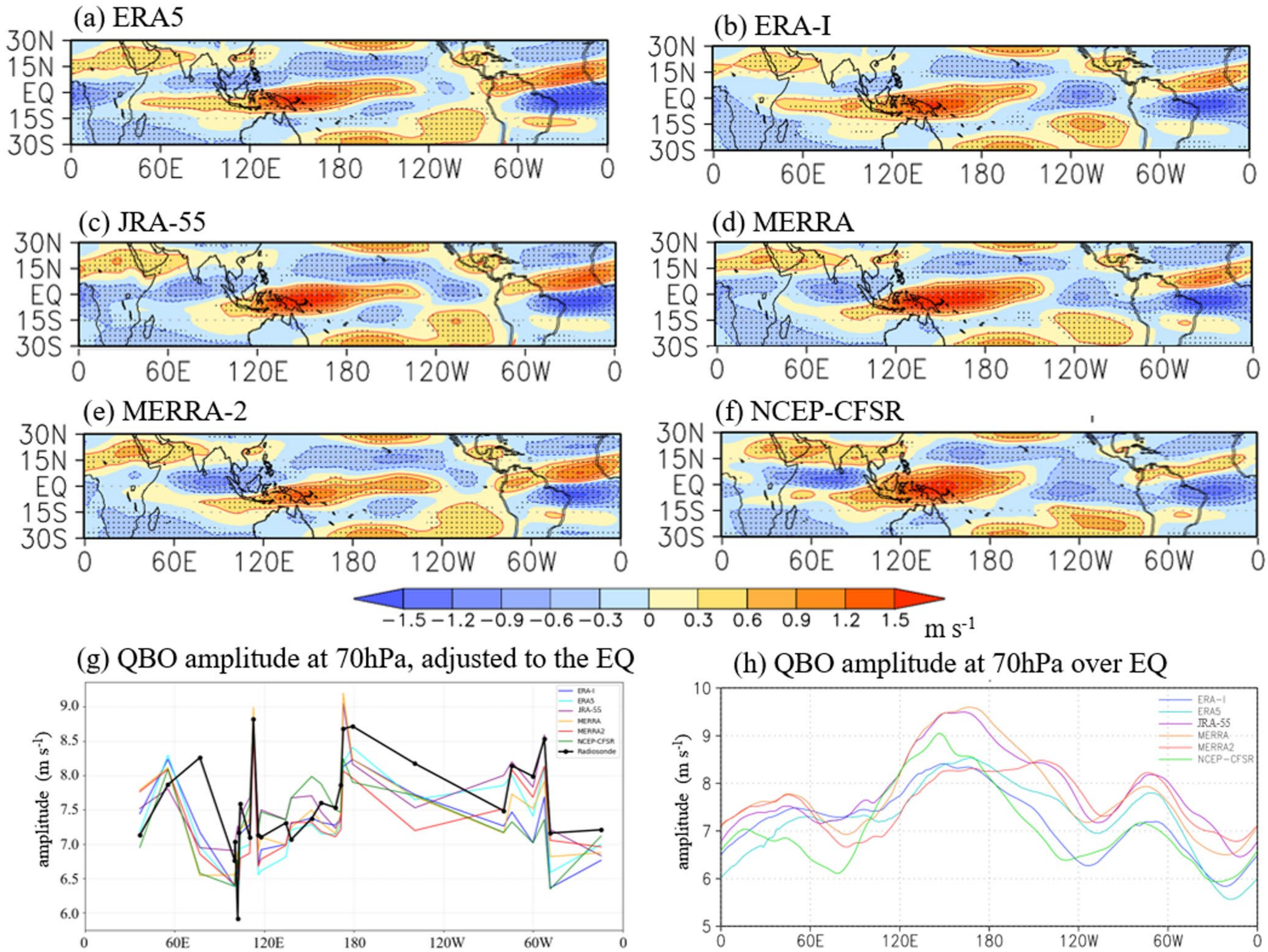

Fig. 6 (**a-f**) Same as Fig. 2d, but for (**a**) ERA5, (**b**) ERA-Interim, (**c**) JRA-55, (**d**) MERRA, (**e**) MERRA-2, and (**f**) NCEP-CFSR. Only regions statistically significant at the 95% confidence level are shaded. Both contour and color intervals are 0.3 m s^{-1}. (**g**) Same as the upper panel of Fig. 5c, but additionally showing QBO amplitudes from six reanalysis datasets. For each reanalysis, the 70-hPa amplitude was interpolated to the 27 IGRA station locations and converted to equivalent equatorial values. (**h**) Longitudinal variations of the 70-hPa QBO amplitude along the equator for the six reanalysis datasets. Corresponding zonal-mean (symmetric) and deviation (asymmetric) components for panels (**g**) and (**h**) are summarized in Supplementary Figs. S5 and S6, respectively

Detailed investigation of the mechanisms maintaining the longitudinal asymmetry of the 70-hPa QBO amplitude, including the influence of background flow, longitudinal variations in wave forcing, and wave–mean flow interactions (e.g., Kawatani et al. 2010) requires analyses with higher frequency data. The radiosonde and reanalysis evidence shows that this asymmetry is robust. Moreover, both CMIP6 and the QBOi multi-model means reproduce the western–central Pacific maximum, and the contrast between QBOi experiments 1 and 2 confirms the ENSO origin of the 150-hPa peak, further supporting the robustness of this asymmetry across independent datasets.

In summary, the QBO amplitude at 70 hPa exhibits significant and robust zonal asymmetry. This asymmetry is apparent in both reanalysis and radiosonde datasets. The consistency between models and reanalyses suggests that both datasets may be useful in future work to investigate the underlying dynamical mechanisms and to examine how this longitudinal structure may affect teleconnections. Further research will be necessary to quantify its impact on convection, large-scale circulation, and teleconnections, and to examine the processes that maintain these longitudinal differences.

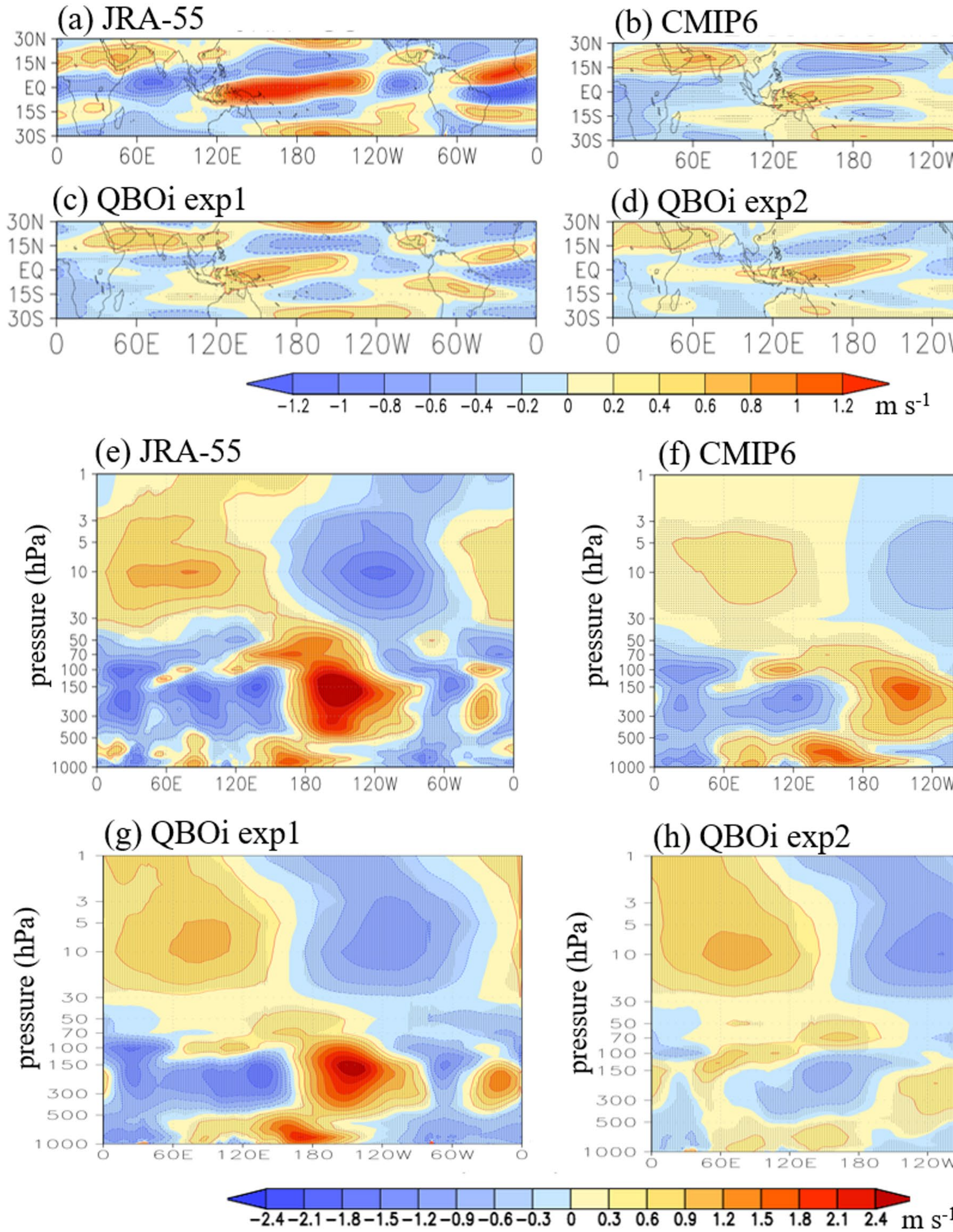

Fig. 7 (**a**–**d**) Same as Fig. 2d, but for the multi-model means of (**b**) CMIP6, (**c**) QBOi experiment 1, and (**d**) QBOi experiment 2, together with (**a**) JRA-55. The color interval is 0.2 m s⁻¹. (**e**–**h**) Same as Fig. 2e, but for the multi-model means of (**f**) CMIP6, (**g**) QBOi experiment 1, and (**h**) QBOi experiment 2, together with (**e**) JRA-55. The color interval is 0.3 m s⁻¹. Stippling denotes regions of statistically significant anomalies at 95% confidence level, evaluated relative to inter-cycle variability for JRA-55 and relative to inter-model spread for CMIP6 and QBOi

Supplementary Information The online version contains supplementary material available at https://doi.org/10.1007/s44393-025-00010-y.

Acknowledgements We thank Prof. K. Hamilton for valuable discussion and helpful comments on the manuscript. YK was supported by Japan Society for Promotion of Science (JSPS) KAKENHI Grant Numbers 23K22574 and 25K01058, by the Environment Research and Technology Development Fund (JPMEERF20242001) of the Environmental Restoration and Conservation Agency of Japan, and by MEXT program for the advanced studies of climate change projection (SENTAN) Grant Number JPMXD0722680395.

Author Contributions R.H. processed the IGRA radiosonde data, conducted the analyses, and prepared the figures and tables. Y.K. designed the study, performed additional analyses, and contributed to the interpretation of the results. R.H. and Y.K. wrote the manuscript together. All authors reviewed the manuscript.

Data Availability The datasets analyzed in this study are publicly available. JRA-55 reanalysis data can be accessed at https://jra.kishou.go.jp/JRA-55/index_en.html. ERA5 reanalysis data are available from ECMWF via https://www.ecmwf.int/en/forecasts/dataset/ecmwf-reanalysis-v5. ERA-Interim reanalysis data are available via ECMWF at https://www.ecmwf.int/en/about/media-centre/news/2008/era-interim-products-available. MERRA reanalysis data can be accessed at https://gmao.gsfc.nasa.gov/gmao-products/merra/. MERRA-2 reanalysis data are available at https://gmao.gsfc.nasa.gov/gmao-products/merra-2/data-access_merra-2/. NCEP-CFSR reanalysis data are available from NCAR RDA at https://rda.ucar.edu/datasets/ds093.0/. IGRA radiosonde data are available from NOAA NCEI at https://www.ncei.noaa.gov/products/weather-balloon/integrated-global-radiosonde-archive. Radiosonde observations from the Integrated Global Radiosonde Archive version 2 (IGRA2) are available from NOAA NCEI at https://www.ncei.noaa.gov/products/weather-balloon/integrated-global-radiosonde-archive. The CMIP6 model output used in this study is publicly available via the Earth System Grid Federation (ESGF) portals (https://esgf-node.llnl.gov/search/cmip6/). The QBO data were historically maintained and distributed by the Free University of Berlin (Naujokat 1986) and are now provided by the Karlsruhe Institute of Technology at https://www.atmohub.kit.edu/english/807.php. Storage for the QBOi multi-model dataset is provided by the Centre for Environmental Data Analysis (CEDA), whose data and processing service is called JASMIN. The NINO3 index used in this study is provided by the Japan Meteorological Agency and is available at https://www.data.jma.go.jp/cpd/data/elnino/index/nino3irm.html.

Declarations

Competing Interests The authors declare no competing interests.

References

Anstey JA, Osprey SM, Alexander J, Baldwin MP, Butchart N, Gray L, Kawatani Y, Newman PA, Richter JH (2022) The quasi-biennial oscillation: Impacts, processes, and projections. Nat Rev Earth Environ. https://doi.org/10.1038/s43017-022-00323-7

Baldwin MP, Gray LJ, Dunkerton TJ, Hamilton K, Haynes PH, Randel WJ, Holton JR, Alexander MJ, Hirota I, Horinouchi T, Jones DBA, Kinnersley JS, Marquardt C, Sato K, Takahashi M (2001) The quasi-biennial oscillation. Rev Geophys 39:179–229. https://doi.org/10.1029/1999RG000073

Butchart N, Anstey J, Hamilton K, Osprey S, McLandress C, Bushell A, Kawatani Y, Kim Y-H, Lott F, Scinocca J, Stckdale T, Bellprat O, Braesicke P, Cangazzo B, Chen C-C, Chun H-Y, Dobrynin M, Garcia R, Garcia-Serrano J, Gray L, Holt L, Kerzenmacher T, Naoe H, Pohlmann H, Ritcher J, Scaife A, Schenzinger V, Serva F, Versick S, Watanabe S, Yoshida K, Yukimoto S (2018) Overview of experiment design and comparison of models participating in the SPARC quasi-biennial oscillation initiative (QBOi). Geosci Model Dev 11:1009–1032. https://doi.org/10.5194/gmd-11-1009-2018

Dee DP, and coauthors (2011) The ERA-Interim reanalysis: configuration and performance of the data assimilation system. Q J R Meteorol Soc 137:553–597

Dunkerton TJ, Delisi DP (1985) Climatology of the equatorial lower stratosphere. J Atmos Sci 42:376–396

Durre I, Yin X, Vose RS, Applequist S, Arnfield J, Korzeniewski B, Hundermark B (2016) Integrated global radiosonde archive (IGRA), version 2. NOAA National Centers for Environmental Information. https://doi.org/10.7289/V5X63K0Q

Gelaro R, McCarty Will, Suárez Max J., Todling Ricardo, Molod Andrea, Takacs Lawrence, Randles Cynthia A., Darmenov Anton, Bosilovich Michael G., Reichle Rolf, Wargan Krzysztof, Coy Lawrence, Cullather Richard, Draper Clara, Akella Santha, Buchard Virginie, Conaty Austin, da Silva Arlindo M., Gu Wei, Kim Gi-Kong, Koster Randal, Lucchesi Robert, Merkova Dagmar, Nielsen Jon Eric, Partyka Gary, Pawson Steven, Putman William, Rienecker Michele, Schubert Siegfried D., Sienkiewicz Meta, Zhao Bin (2017) The modern-era retrospective analysis for research and applications, version 2 (MERRA-2). J Climate 30:5419–5454. https://doi.org/10.1175/JCLI-D-16-0758.1

Hamilton K, Hertzog A, Vial F, Stenchikov G (2004) Longitudinal variation of the stratospheric quasi-biennial oscillation. J Atmos Sci 61:383–402

Hersbach H, Bell Bill, Berrisford Paul, Hirahara Shoji, Horányi András, Muñoz-Sabater Joaquín, Nicolas Julien, Peubey Carole, Radu Raluca, Schepers Dinand, Simmons Adrian, Soci Cornel, Abdalla Saleh, Abellan Xavier, Balsamo Gianpaolo, Bechtold Peter, Biavati Gionata, Bidlot Jean, Bonavita Massimo, De Chiara Giovanna, Dahlgren Per, Dee Dick, Diamantakis Michail, Dragani Rossana, Flemming Johannes, Forbes Richard, Fuentes Manuel, Geer Alan, Haimberger Leo, Healy Sean, Hogan Robin J., Hólm Elías, Janisková Marta, Keeley Sarah, Laloyaux Patrick, Lopez Philippe, Lupu Cristina, Radnoti Gabor, de Rosnay Patricia, Rozum Iryna, Vamborg Freja, Villaume Sebastien, Thépaut Jean-Noël (2020) The ERA5 global reanalysis. Q J R Meteorol Soc 146:1999–2049. https://doi.org/10.1002/qj.3803

Ho C, Kim H, Jeong J, Son S (2009) Influence of stratospheric quasi-biennial oscillation on tropical cyclone tracks in the western North Pacific. Geophys Res Lett 36:L06702. https://doi.org/10.1029/2009GL037163

Ju Z, Rao J, Garfinkel CI, Liu Y, Wang Y, Lu Q (2025) Remote impact of the QBO–MJO on early summer precipitation in Eastern Asia: model evidence from CMIP6. Clim Dyn 63:110. https://doi.org/10.1007/s00382-025-07597-9

Kawatani Y, Hamilton K (2013) Weakened stratospheric quasibiennial oscillation driven by increased tropical mean upwelling. Nature 497:478–481. https://doi.org/10.1038/nature12140

Kawatani Y, Sato K, Dunkerton TJ, Watanabe S, Miyahara S, Takahashi M (2010) The roles of equatorial trapped waves and internal inertia-gravity waves in driving the quasi-biennial oscillation. Part I: Zonal mean wave forcing. J Atmos Sci 67:963–980. https://doi.org/10.1175/2009JAS3222.1

Kawatani Y, Hamilton K, Miyazaki K, Fujiwara M, Anstey JA (2016) Representation of the tropical stratospheric zonal wind in global atmospheric reanalyses. Atmos Chem Phys 16:6681–6699

Kobayashi S, Ota Y, Harada Y, Ebita A, Moriya M, Onoda H, Onogi K, Kamahori H, Kobayashi C, Endo H, Miyaoka K, Takahashi K (2015) The JRA-55 reanalysis: general specifications and basic characteristics. J Meteorol Soc Japan 93:5–48. https://doi.org/10.2151/jmsj.2015-001

Naujokat B (1986) An update of the observed quasi-biennial oscillation of the stratospheric winds over the tropics. J Atmos Sci 43:1873–1877

Newman PA, Coy L, Pawson S, Lait LR (2016) The anomalous change in the QBO in 2015–2016. Geophys Res Lett 43:8791–8797

Osprey S, Butchart N, Knight J, Scaife A, Hamilton K, Anstey J, Schenzinger V, Zhang C (2016) An unexpected disruption of the atmospheric quasi-biennial oscillation. Science 353:1424–1427

Rao J, Garfinkel CI, White IP, Schwartz C (2020a) How does the Quasi-Biennial Oscillation affect the boreal winter tropospheric circulation in CMIP5/6 models? J Climate 33:8975–8996. https://doi.org/10.1175/JCLI-D-20-0024.1

Rao J, Garfinkel CI, White IP, Schwartz C (2020b) Impact of the quasi-biennial oscillation on the northern winter stratospheric polar vortex in CMIP5/6 models. J Climate 33:8915–8934. https://doi.org/10.1175/JCLI-D-19-0663.1

Richter JH, Anstey JA, Butchart N, Kawatani Y, Meehl GA, Osprey SM, Simpson IR (2020) Progress in simulating the quasi-biennial oscillation in CMIP models. J Geophys Res Atmos. https://doi.org/10.1029/2019JD032362

Rienecker MM, Suarez MJ, Gelaro R, Todling R, Bacmeister J, Liu E, Bosilovich MG, Schubert SD, Takacs L, Kim G-K, Bloom S, Chen J, Collins D, Conaty A, da Silva A, Gu W, Joiner J, Koster RD, Lucchesi R, Molod A, Owens T, Pawson S, Pegion P, Redder CR, Reichle R, Robertson FR, Ruddick AG, Sienkiewicz M, Woollen J (2011) MERRA: NASA's modern-era retrospective analysis for research and applications. J Climate 24:3624–3648

Saha S, and coauthors (2010) The NCEP climate forecast system reanalysis. Bull Amer Meteor Soc 91:1015–1057

Sakazaki T, Hamilton K (2022) Discovery of quasi-stationary equatorial waves trapped in stratospheric QBO westerly and easterly jets. J Geophys Res Atmos 127:e2021JD035670. https://doi.org/10.1029/2021JD035670

Seo J, Choi W, Youn D, Park D-SR, Kim J-Y (2013) Relationship between the stratospheric quasi-biennial oscillation and the spring rainfall in the western North Pacific. Geophys Res Lett 40:5949–5953. https://doi.org/10.1002/2013GL058266

Wang Y, Rao J, Lu X, Ju Z, Luo J (2023) A revisit and comparison of the quasi-biennial oscillation disruption events in 2015/16 and 2019/20. Atmos Res 294:106970. https://doi.org/10.1016/j.atmosres.2023.106970

Wang Y, Rao J, Lu Y, Ju Z (2025) QBO disruption–like events in the China Meteorological Administration climate model. Adv Atmos Sci 42:1813–1832. https://doi.org/10.1007/s00376-025-4338-4

Yoo C, Son S-W (2016) Modulation of the boreal wintertime Madden–Julian oscillation by the stratospheric quasi-biennial oscillation. Geophys Res Lett 43:1392–1398. https://doi.org/10.1002/2016GL067762